A semi-analytical scheme to estimate Secchi-disk depth from Landsat-8 measurements

Zhongping Lee,[1,*] Shaoling Shang,[2,*] Lin Qi[1], Jing Yan[2], Gong Lin[2]

[1] School for the Environment, University of Massachusetts Boston, Boston, MA 02125

[2] State Key Lab of Marine Environmental Science, Xiamen University, Xiamen 361005, China

* Corresponding joint authors. Email: zhongping.lee@umb.edu, slshang@xmu.edu.cn.

Abstract

The newly developed semi-analytical scheme (Lee et al. 2015a) for remote sensing of the Secchi disk depth (Z_{SD}, m) was modified and applied to Landsat-8 data to obtain high-spatial-resolution map of water clarity. In order to implement the quasi-analytical algorithm (QAA) for the derivation of absorption and backscattering coefficients from Landsat-8 data, which are key optical properties for the estimation of Z_{SD}, the representative wavelengths of Landsat-8 bands in the visible domain are verified; so are the absorption and backscattering coefficients of pure water for these bands. This semi-analytical scheme was then applied to a dataset having both *in situ* measurements of Z_{SD} (~0.1-30 m) and remote-sensing reflectance and found that the estimated Z_{SD} from remote sensing matches measured Z_{SD} very well (R^2 = 0.96, average absolute percent difference ~17%, N = 197). This scheme was further applied to a Landsat-8 image collected in an estuary to obtain high-spatial resolution Z_{SD} map, and the obtained spatial distribution of Z_{SD} is found quite consistent with *in situ* measurements and visual observations. These results indicate an important application of Landsat data - to provide reliable high-resolution water clarity product of bays, estuaries, and lakes with a unified mechanistic system.

Keywords: water clarity, Secchi disk depth, Landsat-8, semi-analytical algorithm, inherent optical properties

1. Introduction

Coastal and inland waters are important ecosystems for all lives on Earth. They provide important sanctuary for phytoplankton and aquatic animals, resources for recreation activities, and supply of fresh waters for various industries and city dwellers. During the recent decades, from factors of human activities to climate variations, the quality of these water bodies is under significant stress; and there are more and more frequent occurrences of hazardous events, such as harmful algae blooms, in these ecosystems. Adequate, accurate, and consistent monitoring of these water bodies is a high priority for local and federal government agencies.

One of the water quality parameters routinely measured is water clarity (or water transparency) using a Secchi disk (Arnone et al. 1984; Binding et al. 2007; Bukata et al. 1988; Fleming-Lehtinen and Laamanen 2012; Stumpf et al. 1999) - a white or black-and-white disk with a diameter ~30 cm. The depth of this disk when it is no longer viewable by an observer at surface is called the Secchi disk depth (Z_{SD}, m). The value of Z_{SD} provides a direct and intuitive representation of the clarity of a water body; and water clarity is a first order description of the quality status of an aquatic environment, where there have been millions of measurements of Z_{SD} in the past 100+ years in both oceanic and inland water bodies (Boyce et al. 2012). However, due to the inherent limitation from ship surveys, it is infeasible to have adequate and repetitive observations over large areas and/or multiple lakes from shipborne surveys, although it is excellent to provide detailed characterizations of a few isolated locations. Measurements by airborne or space-borne sensors are the only feasible means to achieve large scale and long-term observations of water clarity of aquatic environments.

Satellite systems aimed at water's biogeochemical properties are the ocean color satellite sensors, such as the CZCS of the 1970's and the SeaWiFS/MODIS/MERIS of the 1990's and 2000's (IOCCG 1999). These sensors have a few narrow (~20 nm in bandwidth) spectral bands in the visible domain, and analyses of the radiance measured at these bands can provide quantitative information of water constituents (e.g., concentration of chlorophyll or suspended particulate matter) (IOCCG 2000) and water clarity (Doron et al. 2011; Shang et al. 2010). These systems have a spatial resolution of ~300 m or coarser, which although have shown great applications in coastal zones or large size lakes (Miller and McKee 2004; Petus et al. 2010), run into difficulties to provide adequate measurements for bays, estuaries and many lakes, ecosystems that require much higher spatial resolution for its observations.

The Landsat series (thematic mapper and the enhanced thematic mapper) have 2 or 3 wide (50 nm or more in bandwidth) spectral bands in the visible domain (Roy et al. 2014) which were found useful for the remote sensing of some water constituents that include water clarity (Brezonik et al. 2005; Giardino et al. 2001; Olmanson et al. 2008). In particular, because of the 30 m spatial resolution of the Landsat data, it is "ideal" for synoptic observations of bays and lakes, and a wide range of publications and applications can be found in the literature (Clark et al. 1987; Dekker et al. 2005; Zhang et al. 2003; Zhou et al. 2006). One worthnoting example of such applications is the large scale and long-term monitoring of Z_{SD} of the 10's of thousands of Minnesota lakes from the 20+ years of Landsat data (Olmanson et al. 2008), which show a clear contrast of water clarity of the many lakes and their variations for a two-decade period. The approach used for that effort and many other studies (Binding et al. 2007; Brezonik et al. 2005), however, was purely empirical. Such kind of schemes have two inherent limitations: 1) it requires many and wide range of match-up *in situ* measurements for the derivation of the algorithms coefficients, and; 2) the empirical coefficients are data or location/region dependent, thus the algorithm is not portable for application to other lakes or bays.

To overcome such limitations in empirically retrieving Z_{SD} from remote sensing, it has long been desired to have a mechanistic algorithm for the derivation of Z_{SD} from ocean color measurements. An earlier attempt was that of Doron et al (2011), where the derivation for Z_{SD} was based on a theoretical Z_{SD} model developed from the classical underwater visibility theory (Duntley 1952; Preisendorfer 1986). It was found that, however, the estimated Z_{SD} from ocean color satellite data show large differences when compared with match-up *in situ* measurements (Doron et al. 2011). This poor performance was reviewed in detail recently (Lee et al. 2015a) and it was concluded that the most likely reason for the discouraging results is that the classical model for Z_{SD} does not match the physical processes of sighting a Secchi disk in water by the human eye. A new underwater visibility theory was then proposed and a new mechanistic model for Z_{SD} has been established (Lee et al. 2015a). This model was subsequently evaluated with concurrent measurements (~300 stations, Z_{SD} in a range of ~0.1 - 30 m) of Z_{SD} and remote sensing reflectance in a wide range of environments and obtained an unbiased absolute percent difference of ~18% between model estimated and *in situ* measured Z_{SD} (Lee et al. 2015a), and the difference changes to merely ~23% for a MODIS-*in situ* matchup dataset (where there was a time difference of ± 6 hours between MODIS and *in situ* measurements) [Shang et al, 2015, submitted]. These results indicate a robust performance of the model and algorithm for the estimation of Z_{SD} from ocean color measurements, which further inspired us to extend this mechanistic scheme to Landsat-8 (L8 in the following) data for observation of water clarity of small water bodies. This paper describes the details of estimating Z_{SD} from L8 data, where the remote-sensing reflectance (the input for Z_{SD} estimation) of L8 is generated with Acolite

(Vanhellemont and Ruddick 2015a, b). The overarching goal is to generate Z_{SD} product of bays, estuaries, and lakes with a unified mechanistic data processing system.

2. Methods

2.1 Model of the Secchi-disk depth

Historically, Z_{SD} has been modeled as an inverse function of the beam attenuation coefficient (c) and the diffuse attenuation coefficient (K_d) of downwelling irradiance (Duntley 1952; Preisendorfer 1986). Recently, through a careful and thorough review of the physics of sighting of a Secchi disk by a human eye, it was found that the classical model of Z_{SD} (Aas et al. 2014; Preisendorfer 1986; Zaneveld and Pegau 2004) does not represent the observation of our eyes (Lee et al. 2015a). Following the new underwater visibility theory, the Secchi-disk depth is inversely proportional to the diffuse attenuation coefficient and can be expressed (Lee et al. 2015a)

$$Z_{\mathrm{SD}} = \frac{1}{2.5\,\mathrm{Min}(K_d^{tr})} \ln\left(\frac{\left|0.14 - R_{rs}^{tr}\right|}{0.013}\right). \tag{1}$$

Here K_d^{tr} is the diffuse attenuation coefficient at the transparent window of the water body within the visible domain (410 - 665 nm), with R_{rs}^{tr} the remote-sensing reflectance corresponding to this wavelength. Therefore what is needed for the estimation of Z_{SD} is information of K_d^{tr} from L8 measurements.

2.2 The overall scheme to analytically retrieve IOPs from remote sensing reflectance

Through analytical derivations of the radiative transfer equation, it has been found that K_d is a function of the sun zenith angle and the inherent optical properties (IOPs) (Preisendorfer 1976) of the upper water column, in particular the absorption (a) and backscattering (b_b) coefficients (Gordon 1989; Lee et al. 2013). Thus, the key to obtain K_d^{tr} from L8 measurements is to derive a and b_b from L8 data. Although various analytical or semi-analytical algorithms have been developed in the past decades for the retrieval of IOPs from measurements of ocean color (IOCCG 2006), no such algorithms yet were developed to process Landsat data. Because of the mathematical simplicity and physical transparency, here we adopt the quasi-analytical algorithm (QAA) (Lee et al. 2002) for the retrieval of a and b_b from the remote sensing reflectance of L8 (represented as R_{rs}^{L8}, sr^{-1}), and processing steps are briefly described below.

In general, for R_{rs} observed in the nadir direction, it can be converted to its subsurface counterpart (r_{rs}, sr^{-1}) following (Lee et al. 2002)

$$r_{\mathrm{rs}}(\lambda) = \frac{R_{rs}(\lambda)}{0.52 + 1.7 R_{rs}(\lambda)}. \tag{2}$$

Through modeling of the radiative transfer function, r_{rs} is a function of the ratio of $b_b/(a+b_b)$ and can be expressed as (Gordon et al. 1988)

$$r_{\mathrm{rs}}(\lambda) = \left(g_0 + g_1 \frac{b_b(\lambda)}{a(\lambda) + b_b(\lambda)} \right) \frac{b_b(\lambda)}{a(\lambda) + b_b(\lambda)}. \tag{3}$$

Here g_0 (= 0.089 sr^{-1}) and g_1 (= 0.125 sr^{-1}) are model constants (Lee et al. 2002). From this quadratic function, there is

$$u(\lambda) = \frac{-g_0 + \sqrt{(g_0)^2 + 4 g_1 \times r_{rs}(\lambda)}}{2 g_1}, \tag{4}$$

where $u = b_b/(a+b_b)$. Thus, for any wavelength where there exist measurements of r_{rs}, knowing a will enable the analytical derivation of b_b; vice versa. Following this logic, QAA starts with the estimation of a at a reference wavelength (λ_0)

$$a(\lambda_0) = a_w(\lambda_0) + \Delta a(\lambda_0)\,. \tag{5}$$

Where a_w is the absorption coefficient of pure water and assumed as a constant, $\Delta a(\lambda_0)$ is the contributions from non-water constituents and estimated empirically from r_{rs} spectrum (Lee et al. 2002) [http://www.ioccg.org/groups/software.html].

After $a(\lambda_0)$ is known, $b_b(\lambda_0)$ is solved from Eq. 3 (Lee et al. 2002), which leads to

$$b_{bp}(\lambda_0) = \frac{u(\lambda_0)\times a(\lambda_0)}{1-u(\lambda_0)} - b_{bw}(\lambda_0)\,, \tag{6}$$

where b_{bw} and b_{bp} are the backscattering coefficients of pure seawater and particles, respectively. Further the b_{bp} values at other wavelengths are estimated following a power-law function (Gordon and Morel 1983)

$$b_{bp}(\lambda) = b_{bp}(\lambda_0)\left(\frac{\lambda_0}{\lambda}\right)^{\eta}, \tag{7}$$

with the exponent η estimated empirically from the r_{rs} spectrum [http://www.ioccg.org/groups/software.html]. Since $u(\lambda)$ is available from $r_{rs}(\lambda)$, $a(\lambda)$ can then be easily derived after $b_{bp}(\lambda)$ is known

$$a(\lambda) = (1-u(\lambda))(b_{bw}(\lambda) + b_{bp}(\lambda))/u(\lambda)\,. \tag{8}$$

Following the radiative transfer equation, $K_d(\lambda)$ is a function of $a(\lambda)$ and $b_b(\lambda)$ and can be modeled as(Lee et al. 2013)

$$K_d(\lambda) = (1 + m_0 \times \theta_s) a(\lambda) + \left(1 - \gamma \frac{b_{bw}(\lambda)}{b_b(\lambda)}\right) \times m_1 \times (1 - m_2 \times e^{-m_3 \times a(\lambda)}) b_b(\lambda) \,. \quad (9)$$

Here $m_{0\text{-}3}$ and γ are model parameters and their values are 0.005, 4.26, 0.52, 10.8, and 0.265, respectively. θ_s (in degrees) is the solar zenith angle in air.

2.3 Algorithm parameters for implementing QAA with L8 band setting

For processing hyperspectral or MODIS or SeaWiFS remote sensing measurements, λ_0 is designated as 55x or 670 nm (Lee et al. 2002) [http://www.ioccg.org/groups/software.html], whereas the required values for $a_w(\lambda_0)$ and $b_{bw}(\lambda_0)$ are determined based on a_w and b_{bw} spectra reported in the literature (Morel 1974; Pope and Fry 1997; Zhang et al. 2009). For L8, however, because some bands (Band 2 and Band 3 in particular) have a bandwidth ~60 nm, it is necessary to designate a representative wavelength for each band in order to properly propagate the optical properties from one band to another (e.g., Eq. 7). Also, it is required to determine the corresponding a_w and b_{bw} values for each band in order to implement QAA for L8 data.

The listed center wavelengths for the first four L8 bands are 443, 483, 561, and 655 nm, respectively (Franz et al. 2015; Vanhellemont and Ruddick 2015b). Fundamentally, because the reflectance of each wide band is a weighted average of the corresponding hyperspectral reflectance (see Eq. 10 below), the listed center wavelengths of these L8 bands may not necessarily reflect the representative wavelengths of an interested target if the reflectance of this target is strongly spectral dependent within a spectral window of ~50 nm. To obtain the representative wavelength of L8 bands for aquatic environments, remote sensing reflectance of equivalent L8 bands (R_{rs}^{L8}) of a set (901 spectra) of hyperspectral R_{rs} measured in oceanic and coastal environments (Lee et al. 2014) were calculated by including the response function of each band (Gordon 1995)

$$R_{rs}^{L8}(B_i) = \frac{\int_{400}^{800} R_{rs}(\lambda)\, RSR_i(\lambda)\, d\lambda}{\int_{400}^{800} RSR_i(\lambda)\, d\lambda}. \quad (10)$$

Here RSR_i is the response function of L8 band number i (B_i), and the hyperspectral (400-800 nm, 5-nm resolution) R_{rs} (Lee et al. 2014) were interpolated to 1-nm resolution for this calculation. For each L8 band, the calculated $R_{rs}^{L8}(B_i)$ were then compared with hyperspectral R_{rs} for wavelengths (λ_j) within ± 10 nm of the listed center wavelengths, respectively, and the slope and bias in linear regression were calculated for each pair of $R_{rs}^{L8}(B_i)$ vs $R_{rs}(\lambda_j)$. Table 1 presents results (bias and |slope - 1.0|) of a few of these pairs. Based on these statistical values, it is appeared that the center wavelengths of the L8 visible bands presented in the literature are generally applicable for aquatic environments. For Band 3, however, it is found that the most representative wavelength (slope close to 1.0 and a bias closed to 0) is 554 nm (see Fig. 1), instead of the listed 561 nm (close to 0 bias, but slope is ~0.96), although both wavelengths have a coefficient of determination (R^2) > 0.99 when compared with $R_{rs}^{L8}(B_3)$. This might be in part because the absorption coefficient of pure water increases rapidly (a factor of ~4) from 520 nm to 600 nm (Pope and Fry 1997), and R_{rs} of aquatic environments are generally much higher (at least for this dataset) in the shorter than in the longer wavelengths for wavelength domain of B_3, therefore the spectrally weighted average (Eq. 10) at this band will have a tendency tilting to the shorter wavelength. Without losing the generality and for easy processing of L8 image, 554 nm is employed as the representative wavelength for L8 Band 3 in this effort, although the impact on the estimation of b_{bp} at short wavelengths (see Eq. 7) is generally less than 2% for this modification.

After the verification of the representative wavelengths for the L8 bands in the visible domain, the other parameters required to be determined for the implementation of QAA is $a_w^{L8}(B_i)$ and $b_{bw}^{L8}(B_i)$. Because R_{rs} is proportional to the backscattering coefficient (Eq. 3), band-averaged $b_{bw}^{L8}(B_i)$ of the first four bands were calculated following the scheme to obtain band-averaged R_{rs},

$$b_{bw}^{L8}(B_i) = \frac{\int_{400}^{800} b_{bw}(\lambda)\, RSR_i(\lambda) d\lambda}{\int_{400}^{800} RSR_i(\lambda) d\lambda}, \tag{11}$$

with hyperspectral b_{bw} spectrum from Zhang et al (2009).

On the other hand, because R_{rs} is inversely proportional to the absorption coefficient, band-averaged $a_w^{L8}(B_i)$ were obtained from a two-step process:

$$x_w^{L8}(B_i) = \frac{\int_{400}^{800} RSR_i(\lambda)\left(1/a_w(\lambda)\right) d\lambda}{\int_{400}^{800} RSR_i(\lambda) d\lambda}, \tag{12a}$$

$$a_w^{L8}(B_i) = \frac{1}{x_w^{L8}(B_i)}. \tag{12b}$$

The hyperspectral (5-nm original resolution, interpolated to 1-nm resolution) a_w spectrum for the 400-800 nm range used in the above calculation is a combination of the results of Lee et al

(2015b) (400 - 545 nm), Pope and Fry (1997) (550 - 720 nm), and Kou et al (1993) (725 - 800 nm). The resulted $a_w^{L8}(B_i)$ and $b_{bw}^{L8}(B_i)$ are presented in Table 2.

Further, since there are no significant differences between the representative wavelengths of L8 bands and those of SeaWiFS bands, the default algorithm coefficients used in the current version of QAA [http://www.ioccg.org/groups/software.html] to estimate $\Delta a(\lambda_0)$ were applied for the L8 band settings. With the above-derived a_w and b_{bw} values for L8, a and b_b of the first four L8 bands can be adequately derived from R_{rs}^{L8} following the steps described in Section 2.2; subsequently K_d of these bands can be calculated based on Eq. 9.

2.4 Spectral gap filling

Sighting a Secchi disk in water represents measurements of optical signal in the most transparent window of the water (Aas et al. 2014; Lee et al. 2015a), which was found can be well characterized with measurements around 440, 490, 530, 555, and 670 nm (Lee et al. 2015a). L8, however, has only four wide bands centered at ~443, 481, 554 and 656 nm in the visible domain, thus lacks a band focused at the 500-530 nm window that covers waters more transparent at these wavelengths. Although there is also a wide spectral gap between 554 and 656 nm, extremely few waters having a transparent window in this spectral range, thus this window is not important for the determination of Z_{SD}, as evidenced for the wide range of environments reported in Lee et al (2015a). To fill the spectral gap around 530 nm, we developed an empirical relationship based on the dataset used in Lee et al (2015a). In that study, $K_d(488)$, $K_d(530)$, and $K_d(555)$ were all estimated independently from the measured R_{rs} spectrum; and, through multiple regression analysis, it was found that

$$K_d(530) = 0.20\,K_d(488) + 0.75\,K_d(555)\,. \tag{13}$$

Figure 2 compares Eq. 13 estimated $K_d(530)$ with that derived from $R_{rs}(530)$, where the unbiased average absolute percent difference is ~6.9% (R^2 = 0.99, N = 338). Such results provide us the confidence to estimate $K_d(530)$ from values of $K_d(488)$ and $K_d(555)$. Thus, by assuming no significant difference in attenuation coefficients for the small wavelength differences, $K_d(530)$ for L8 band setting is approximated as

$$K_d^{L8}(530) = 0.20\,K_d^{L8}(481) + 0.75\,K_d^{L8}(554)\,. \tag{14}$$

Therefore, with K_d at 443, 481, 554, and 656 nm retrieved semi-analytically from R_{rs}^{L8}, and $K_d(530)$ estimated from $K_d(481)$ and $K_d(554)$, a spectral minimum K_d of a water body can then be determined from the multiband K_d data, and Z_{SD} can be calculated following Eq. 1. In this calculation, because R_{rs}^{L8} is significantly smaller than the remote-sensing reflectance of a white disk, there was no attempt to find the R_{rs}^{L8} value corresponding to 530 nm, and R_{rs}^{tr} in Eq. 1 was determined as the maximum R_{rs} value among wavelengths of 443, 481, 554, and 656 nm.

3. Results

A dataset of 197 sites (see Fig. 6 of Lee et al (2015a) for locations) containing concurrent measurements of Z_{SD} and hyperspectral R_{rs} is used to evaluate the performance of the above-described semi-analytical scheme to estimate Z_{SD} from L8 band settings. Measurements of Z_{SD} were carried out conventionally with a standard 30 cm white disk. Measurements of hyperspectral R_{rs} were carried out from above the sea surface with a GER 1500 (350 - 1000 nm, 3 nm resolution) following the Ocean Optics Protocols (Mueller et al. 2003), with the processing steps detailed in Shang et al (2011). The equivalent L8 R_{rs} of these measurements were derived following Eq. 10, subsequently a, b_b, and K_d of the L8 bands were derived with the steps described in Section 2.2, which further led to semi-analytically estimated Z_{SD} following Eq. 1. A nominal sun angle of 30° from zenith was used for the calculation of K_d of all stations.

The comparison between Z_{SD} derived from simulated-R_{rs}^{L8} and *in situ* Z_{SD} is shown in Fig. 3. Statistically, the R^2 value in linear regression analysis between the two Z_{SD} datasets (in a range of ~0.1 - 30 m) is 0.96, along with average unbiased absolute percent difference as 16.7%. These results are almost identical to that obtained from multispectral narrow-bandwidth R_{rs} (see Fig. 6 of Lee et al (2015a)), suggesting robust Z_{SD} retrievals from R_{rs}^{L8}. This may not be too surprising because Z_{SD} value represents a measurement of the bulk water property, whereas the band settings of L8 also provide an observation the bulk water. It deserves an emphasis, however, that during this evaluation there was no algorithm tuning to fit the measured Z_{SD} values for the wide range of environments encountered. It is the same algorithm used for the derivation of Z_{SD} for all locations covering clear oceanic and turbid coastal waters. Such features ensure reliable and consistent Z_{SD} retrievals from R_{rs}^{L8} for different regions or areas as long as the quality of R_{rs}^{L8} derived from L8 images is acceptable. On the other hand, it is necessary to point out that the upper limit of this Z_{SD} dataset is ~30 m, thus not so sure yet of the potentials of using L8 to monitor Z_{SD} of super blue waters where the transparent window might be in the 400-450 nm range, a window not clear if L8 has enough signals from such waters.

4. Demonstration with a Landat-8 image

The scheme described in Section 2 was applied to an L8 image to obtain a high-spatial resolution (30 m) water clarity map of an estuary, whereas the sensor specifics of L8 can be found in Roy et al (2014) and Franz et al (2015). This image (LC81190432013216LGN00) was collected on August 4, 2013 and the targeted area is the Jiulongjiang River estuary off Xiamen city, China (see Fig. 4a and Fig. 4b for the location). The selection of this L8 image was because that there were measurements of both Z_{SD} and hyperspectral remote sensing reflectance in this area (the three red circles in Fig. 4b) eleven days ago (July 24, 2013), with Z_{SD} as 0.4, 0.8, and 1.4 m at P1, P2 and P3, respectively.

The analytical approach to retrieve Z_{SD} requires R_{rs}^{L8} as inputs, which was generated with the Acolite algorithm detailed in Vanhellemont and Ruddick (2015b). As a crude evaluation of the quality of R_{rs} retrieved with Acolite, Fig. 4c shows R_{rs}^{L8} from L8 and R_{rs}^{L8} calculated from hyperspectral R_{rs} of the three points marked in Fig. 4b. Because there was an 11-day temporal gap between the L8 observation and *in situ* measurements and this is a highly dynamic estuary, there are obvious differences in R_{rs} values (especially at P1), but overall R_{rs}^{L8} appeared valid and consistent with this turbid aquatic system. And, all three locations have the maximum R_{rs}^{L8} at Band 3; because K_d is generally dominated by a and R_{rs} is inversely proportional to a, these R_{rs}^{L8} spectra indicate that the K_d values at Band 3 were used for the estimation of Z_{SD} of these locations.

The Z_{SD} map of this area derived from L8 is shown in Fig. 4d. Generally there is a pattern of higher clarity (~2 m) further offshore while lower clarity (< ~0.3 m) closer to the river mouth; and the Jiulongjiang River has a water clarity generally less than 0.2 m - spatial patterns that are consistent with numerous visual observations of tourists and fishermen. For locations P1, P2 and

P3, Z_{SD} values from the L8 data are ~0.3, ~0.6, and ~0.9 m, respectively; which are ~0.2, ~0.7, and ~1.3 m, respectively, from *in situ* hyperspectral R_{rs}. The *in situ* and L8 Z_{SD} values do not exactly match each other; but the spatial gradient, i.e. an increase of Z_{SD} from the inner estuary to the outer estuary, is consistent. There are certainly uncertainties associated with the Z_{SD} algorithm (Lee et al. 2010; Lee et al. 2015a) and that of the derived R_{rs} from L8 measurements (Vanhellemont and Ruddick 2015b), which will contribute to the Z_{SD} difference. However, the primary source of difference in the Z_{SD} values here is most probably due to the gap in observation time (11 days). The Jiulongjiang River estuary is an area with a semi-diurnal tide; clearer sea water goes upstream at high tide, while turbid river water covers most of the estuary at low tide. Z_{SD} at a locale could thus change within hours even in a day.

5. Conclusions

It is found that the spectral band setting of Landsat-8 is adequate for the estimation of Secchi disk depth (Z_{SD}); and the accuracy of the semi-analytically estimated Z_{SD} from L8 band setting is similar to that obtained from a SeaWiFS/MODIS-type dataset, at least for Z_{SD} in a range of ~0.1 - 30 m. These results provide an indirect support on the retrieval of water's total absorption and backscattering coefficients from L8 band settings with the quasi-analytical algorithm (Lee et al. 2002) [http://www.ioccg.org/groups/software.html]. Further, as a demonstration, an application of the semi-analytical scheme for Z_{SD} to an L8 image collected over a turbid estuarine area obtained reasonable Z_{SD} values and consistent spatial patterns. These results suggest that the Acolite algorithm for atmosphere correction of Landsat-8 image (Vanhellemont and Ruddick 2015b) is promising and support further the semi-analytical scheme for Z_{SD} from L8 data.

However, because the quality of R_{rs} plays a critical role on the quantitative remote sensing of water properties, it demands substantial efforts from the community to develop robust processing systems to generate high-quality R_{rs} from L8 for various lake and estuary ecosystems; which also demands support and efforts to obtain more concurrent measurements to validate the R_{rs} and Z_{SD} products from L8.

Acknowledgements:

Financial support was provided by the National Aeronautic and Space Administration (NASA) Ocean Biology and Biogeochemistry and Water and Energy Cycle Programs (Lee), the National Oceanic and Atmospheric Administration (NOAA) JPSS VIIRS Ocean Color Cal/Val Project (Lee), United States Geological Survey (Lee), the National Natural Science Foundation of China (No. 41376177, Shang) and Ministry of Science and Technology of China (No. 2013BAB04B00, Shang), and the University of Massachusetts Boston. We thank Quinten Vanhellemont for sharing the Acolite L8 atmosphere correction code.

References:

Aas, E., Høkedal, J., & Sørensen, K. (2014). Secchi depth in the Oslofjord–Skagerrak area: theory, experiments and relationships to other quantities. Ocean Sciences **10**: 177-199

Arnone, R.A., Tucker, S.P., & Hilder, F.A. (1984). Secchi Depth Atlas Of The World Coastlines. In, *Ocean Optics VII, Proc. SPIE 0489* (p. doi:10.1117/1112.943305). Monterey, CA

Binding, C.E., Jerome, J.H., Bukata, R.P., & Booty, W.G. (2007). Trends in Water Clarity of the Lower Great Lakes from Remotely Sensed Aquatic Color. J. Great Lakes Res. **33**: 828-841

Boyce, D.G., Lewis, M., & Worm, B. (2012). Integrating global chlorophyll data from 1890 to 2010. Limnol. Oceanogr.: Methods **10**: 840–852

Brezonik, P., Menken, K.D., & Bauer, M. (2005). Landsat-based Remote Sensing of Lake Water Quality Characteristics, Including Chlorophyll and Colored Dissolved Organic Matter (CDOM). Lake and Reservoir Management **21**: 373-382

Bukata, R.P., Jerome, J.H., & Bruton, J.E. (1988). Relationships among Secchi disk depth, beam attenuation coefficient, and irradiance attenuation coefficient for Great Lakes waters. J. Great Lakes Res. **14**: 347-355

Clark, R.K., Fay, T.H., & Walker, C.L. (1987). Bathymetry calculations with Landsat 4 TM imagery under a generalized ratio assumption. Applied Optics **26**: 4036-4038

Dekker, A.G., Brando, V.E., & Anstee, J.M. (2005). Retrospective seagrass change detection in a shallow coastal tidal Australian lake. Remote Sensing of Environment **97**: 415-433

Doron, M., Babin, M., Hembise, O., Mangin, A., & Garnesson, P. (2011). Ocean transparency from space: Validation of algorithms using MERIS, MODIS and SeaWiFS data. Remote Sensing of Environment **115**: 2986-3001

Duntley, S.Q. (1952). The visibility of submerged objects. In, *Visibility Lab., Mass. Inst. Tech.* (p. 74). San Diego

Fleming-Lehtinen, V., & Laamanen, M. (2012). Long-term changes in Secchi depth and the role of phytoplankton in explaining light attenuation in the Baltic Sea. Estuarine, Coastal and Shelf Science **102-103**: 1-10

Franz, B.A., Bailey, S.W., Kuring, N., & Werdell, P.J. (2015). Ocean color measurements with the Operational Land Imager on Landsat-8: implementation and evaluation in SeaDAS. J. Appl. Rem. Sens. **9**: 1-16

Giardino, C., Pepe, M., Brivio, P.A., Ghezzi, P., & Zilioli, E. (2001). Detecting chlorophyll, Secchi disk depth and surface temperature in a sub-alpine lake using Landsat imagery. Science of the Total Environment **268**: 19-29

Gordon, H. (1995). Remote sensing of ocean color: a methodology for dealing with broad spectral bands and significant out-of-band response. Applied Optics **34**: 8363-8374

Gordon, H.R. (1989). Can the Lambert-Beer law be applied to the diffuse attenuation coefficient of ocean water? Limnol. Oceanogr. **34**: 1389-1409

Gordon, H.R., Brown, O.B., Evans, R.H., Brown, J.W., Smith, R.C., Baker, K.S., & Clark, D.K. (1988). A semianalytic radiance model of ocean color. J. Geophys. Res. **93**: 10,909-910,924

Gordon, H.R., & Morel, A. (1983). *Remote assessment of ocean color for interpretation of satellite visible imagery: A review*. New York: Springer-Verlag

IOCCG (1999). Status and plans for satellite ocean-color missions: Considerations for complementary missions. In J.A. Yoder (Ed.), *Reports of the International Ocean-Colour Coordinating Group, No.2*. Halifax, Canada: IOCCG

IOCCG (2000). Remote Sensing of Ocean Colour in Coastal, and Other Optically-Complex, Waters. In S. Sathyendranath (Ed.), *Reports of the International Ocean-Colour Coordinating Group, No.3*. Dartmouth, Canada: IOCCG

IOCCG (2006). Remote Sensing of Inherent Optical Properties: Fundamentals, Tests of Algorithms, and Applications. In Z.-P. Lee (Ed.), *Reports of the International Ocean-Colour Coordinating Group, No. 5* (p. 126). Dartmouth, Canada: IOCCG

Kou, L., Labrie, D., & Chylek, P. (1993). Refractive indices of water and ice in the 0.65- to 2.5-μm spectral range. Applied Optics **32**: 3531-3540

Lee, Z.P., Carder, K.L., & Arnone, R. (2002). Deriving inherent optical properties from water color: A multi-band quasi-analytical algorithm for optically deep waters. Applied Optics **41**: 5755-5772

Lee, Z.-P., Arnone, R., Hu, C., Werdell, P.J., & Lubac, B. (2010). Uncertainties of optical parameters and their propagations in an analytical ocean color inversion algorithm. Applied Optics **49**: 369-381

Lee, Z.P., Hu, C., Shang, S., Du, K., Lewis, M., Arnone, R., & Brewin, R. (2013). Penetration of UV-Visible solar light in the global oceans: Insights from ocean color remote sensing. J. Geophys. Res. **118**: 4241-4255, doi:4210.1002/jgrc.20308

Lee, Z., Shang, S., Hu, C., & Zibordi, G. (2014). Spectral interdependence of remote-sensing reflectance and its implications on the design of ocean color satellite sensors. Appl. Opt. **53**: 3301-3310

Lee, Z., Shang, S., Hu, C., Du, K., Weidemann, A., Hou, W., Lin, J., & Lin, G. (2015a). Secchi disk depth: A new theory and mechanistic model for underwater visibility. Rem. Sens. Enviro. **169**: 139-149

Lee, Z., Wei, J., Voss, K., Lewis, M., Bricaud, A., & Huot, Y. (2015b). Hyperspectral absorption coefficient of “pure” seawater in the range of 350–550 nm inverted from remote sensing reflectance. Applied Optics **54**: 546-558

Miller, R.L., & McKee, B.A. (2004). Using MODIS 250 m imagery to map concentrations of total suspended matter in coastal waters. Remote Sens. Environ. **93**: 259-266

Morel, A. (1974). Optical properties of pure water and pure sea water. In N.G. Jerlov, and Nielsen, E. S. (Ed.), *Optical Aspects of Oceanography* (pp. 1-24). New York: Academic

Mueller, J.L., Fargion, G.S., & McClain, C.R. (2003). Ocean Optics Protocols For Satellite Ocean Color Sensor Validation, Revision 4. In. Goddard Space Flight Center, Greenbelt, MD: NASA

Olmanson, L.G., Bauer, M.E., & Brezonik, P.L. (2008). A 20-year Landsat water clarity census of Minnesota's 10,000 lakes. Remote Sensing of Environment **112**: 4086-4097

Petus, C., Chust, G., Gohin, F., Doxaran, D., Froidefond, J.M., & Sagarminaga, Y. (2010). Estimating turbidity and total suspended matter in the Adour River plume (South Bay of Biscay) using MODIS 250-m imagery. Continental Shelf Research **30**: 379-392

Pope, R., & Fry, E. (1997). Absorption spectrum (380 - 700 nm) of pure waters: II. Integrating cavity measurements. Applied Optics **36**: 8710-8723

Preisendorfer, R.W. (1976). *Hydrologic optics vol. 1: introduction*. Springfield: National Technical Information Service. Also available on CD, Office of Naval Research

Preisendorfer, R.W. (1986). Secchi disk science: Visual optics of natural waters. Limnol. Oceanogr. **31**: 909-926

Roy, D.P., Wulder, M.A., T.R.Loveland, Woodcock, C., Allen, R., Anderson, M.C., Helder, D., Irons, J.R., Johnson, D.M., Kennedy, R., Scambos, T.A., Schaaf, C.B., Schott, J.R., Sheng, Y., Vermote, E.F., Belward, A.S., Bindschadler, R., Cohen, W.B., Gao, F., Hipple, J.D., Hostert, P., Huntington, J., Justice, C.O., Kilic, A., Kovalskyy, V., Lee, Z.P., Lymburner, L., Masek, J.G., McCorkel, J., Shuai, Y., Trezza, R., Vogelmann, J., Wynne, R.H., & Zhu, Z.

(2014). Landsat-8: Science and product vision for terrestrial global change research. Rem. Sens. Enviro. **145**: 154-172

Shang, S., Lee, Z., & Wei, G. (2010). Characterization of Satellite-Derived Euphotic Zone Depth: Results for the China Sea. Remote Sensing of Environment **115**: 180-186

Shang, S.L., Dong, Q., Lee, Z.P., Li, Y., Xie, Y.S., & Behrenfeld, M.J. (2011). MODIS Observed Phytoplankton Dynamics in the Taiwan Strait: an Absorption-based Analysis. Biogeosciences **8**: 841-850

Stumpf, R.P., Frayer, M.L., Durako, M.J., & Brock, J.C. (1999). Variations in water clarity and bottom albedo in Florida Bay from 1985 to 1997. Estuaries **22**: 431-444

Vanhellemont, Q., & Ruddick, K. (2015a). Advantages of high quality SWIR bands for ocean colour processing: Examples from Landsat-8. Remote Sens. Env. **145**: 89-106

Vanhellemont, Q., & Ruddick, K. (2015b). Turbid wakes associated with offshore wind turbines observed with Landsat 8. Rem. Sens. Enviro. **145**: 105-115

Zaneveld, J.R., & Pegau, W.S. (2004). Robust underwater visibility parameter. Optics Express **11**: 2997-3009

Zhang, X., Hu, L., & He, M.-X. (2009). Scattering by pure seawater: Effect of salinity. Optics Express **17**: 5698-5710

Zhang, Y., Pulliainen, J.T., Koponen, S.S., & Hallikaine, M.T. (2003). Water Quality Retrievals From Combined Landsat TM Data and ERS-2 SAR Data in the Gulf of Finland. IEEE TRANSACTIONS ON GEOSCIENCE AND REMOTE SENSING **41**: 622-629

Zhou, W., Wang, S., Zhou, Y., & Troy, A. (2006). Mapping the concentrations of total suspended matter in Lake Taihu, China, using Landsat-5 TM data. International Journal of Remote Sensing **27**: 1177-1191

Figure captions:

Figure 1. Relationship between $R_{rs}^{L8}(B3)$ and R_{rs}(554;561) for a wide range of aquatic environments.

Figure 2. K_d(530) synthesized from K_d(488) and K_d(555) compared with K_d(530) derived from R_{rs}(530).

Figure 3. Comparison between Z_{SD} derived from simulated R_{rs}^{L8} and *in situ* Z_{SD}. The average unbiased absolute percent difference is ~17% with Z_{SD} in a range of ~0.1 - 30 m.

Figure 4. Application of the semi-analytic Z_{SD} scheme to an L8 image over the estuary off Xiamen City, China. (a) Location of the targeted area. (b) Pseudo true color of the estuary from the L8 measurements. (c) R_{rs}^{L8} from L8 compared with that from *in situ* measurements for the three red points in (b); solid lines for R_{rs}^{L8} from *in situ* measurements, open symbols for R_{rs}^{L8} from L8. Note that there is an 11-day gap between the two observations. (d). Z_{SD} map derived from R_{rs}^{L8}.

Table 1. Representative wavelength of Landsat-8 visible bands

Band 1 (433-453 nm)					
Wavelength [nm]	441	442	**443**	444	445
|Slope-1|	0.0042	0.0016	**0.0014**	0.0047	0.0084
bias	0.00001	0.00001	**0.00001**	0.00002	0.00002
Band 2 (450-515 nm)					
Wavelength [nm]	480	**481**	482	483	484
|Slope-1|	0.0079	**0.0025**	0.0028	0.0082	0.0137
bias	-0.00015	**-0.00013**	-0.00012	-0.00011	-0.00009
Band 3 (525-600 nm)					
Wavelength [nm]	553	**554**	555	556	557
|Slope-1|	0.0039	**0.0003**	0.0048	0.0094	0.0143
bias	-0.00022	**-0.00020**	-0.00018	-0.00016	-0.00015
Band 4 (630-680 nm)					
Wavelength [nm]	654	655	**656**	657	658
|Slope-1|	0.0176	0.0099	**0.0011**	0.0089	0.0195
bias	0.00000	0.00001	**0.00002**	0.00004	0.00005

Table 2. Absorption and backscattering coefficients of pure seawater for L8 visible bands.

	Band 1	Band 2	Band 3	Band 4
a_w (m^{-1})	0.005	0.011	0.064	0.368
b_{bw} (m^{-1})	0.0021	0.0014	0.0008	0.0004

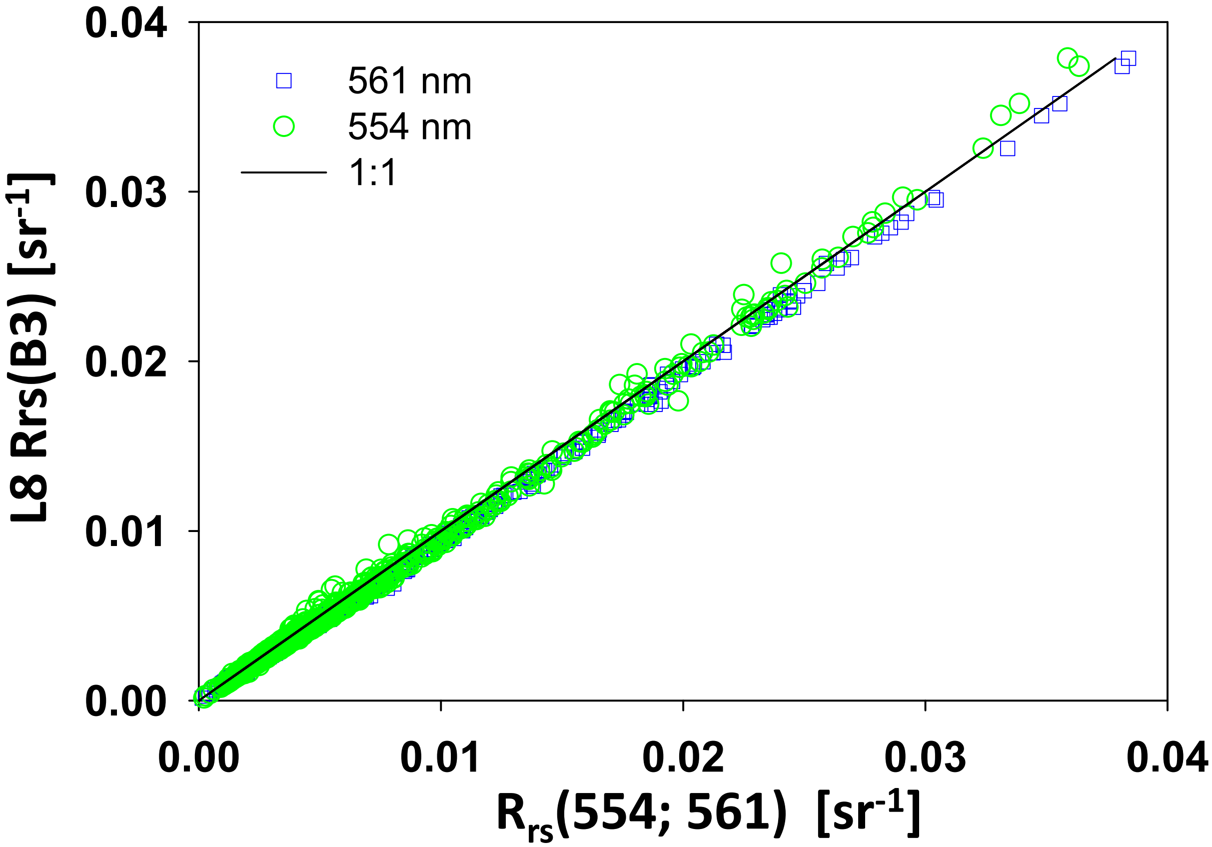

Figure 1. Relationship between $R_{rs}^{L8}(B3)$ and R_{rs}(554;561) for a wide range of aquatic environments.

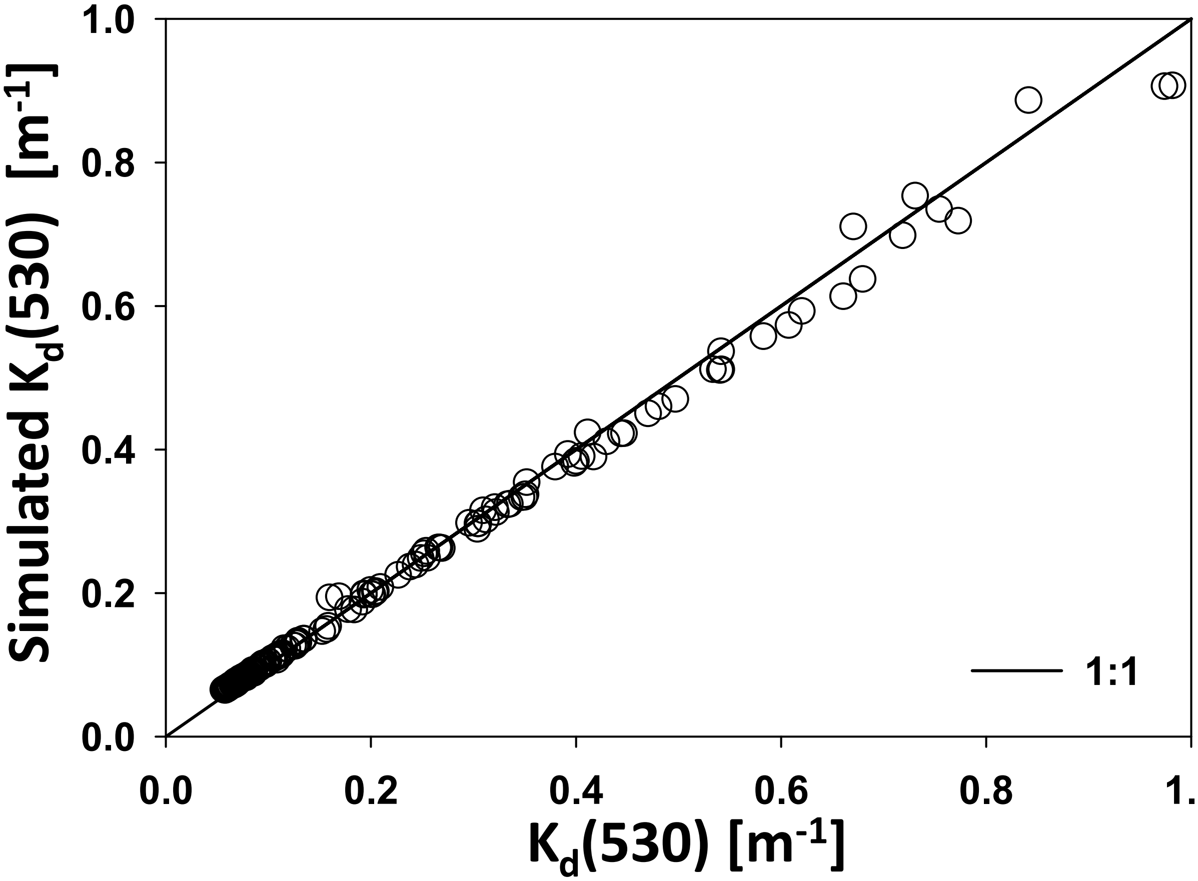

Figure 2. K_d(530) synthesized from K_d(488) and K_d(555) compared with K_d(530) derived from R_{rs}(530).

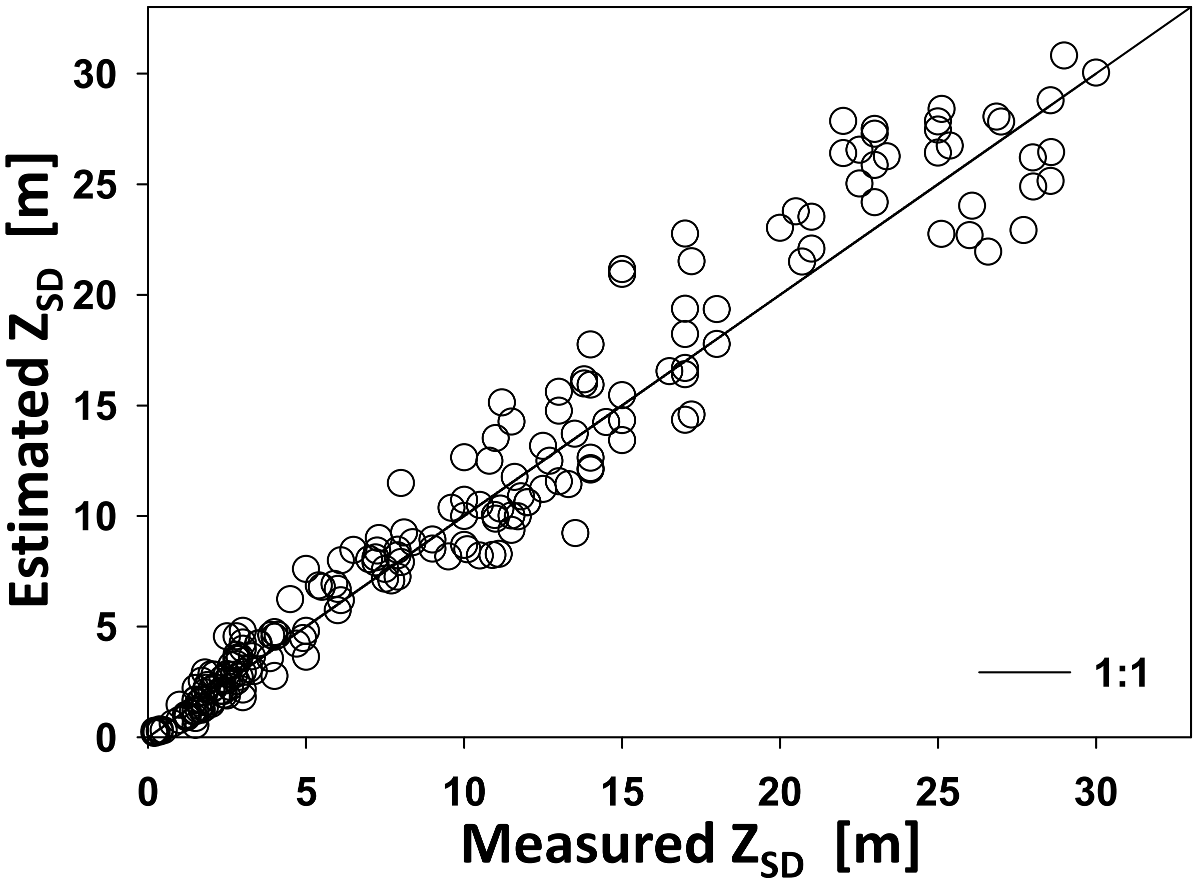

Figure 3. Comparison between Z_{SD} derived from simulated R_{rs}^{L8} and *in situ* Z_{SD}. The average unbiased absolute percent difference is ~17% with Z_{SD} in a range of ~0.1 - 30 m.

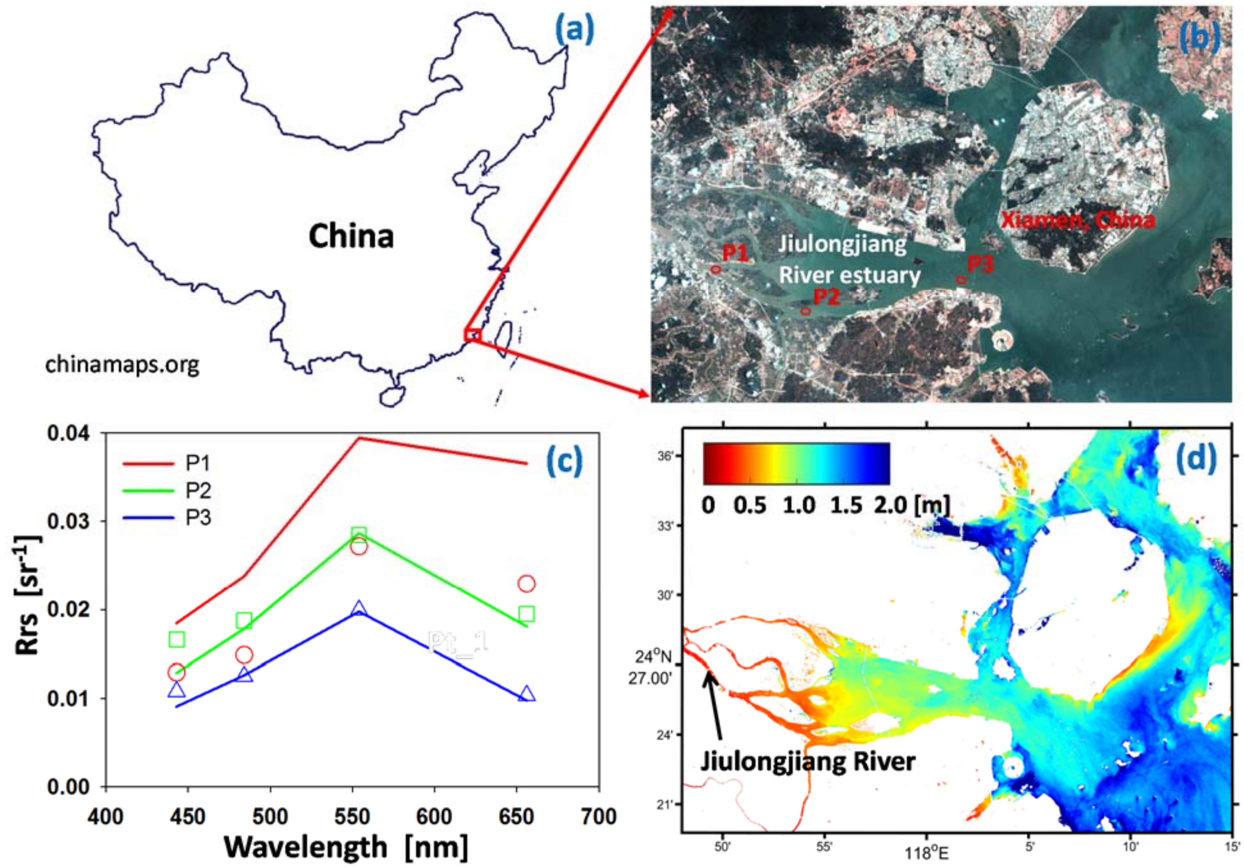

Figure 4. Application of the semi-analytic Z_{SD} scheme to an L8 image over the estuary off Xiamen City, China. (a) Location of the targeted area. (b) Pseudo true color of the estuary from the L8 measurements. (c) R_{rs}^{L8} from L8 compared with that from *in situ* measurements for the three red points in (b); solid lines for R_{rs}^{L8} from *in situ* measurements, open symbols for R_{rs}^{L8} from L8. Note that there is an 11-day gap between the two observations. (d). Z_{SD} map derived from R_{rs}^{L8}.